# An Improved Theoretical Model to Explain Electronic and Optical Properties of p-Type GaAs/AlGaAs Superlattices for Multi-Wavelength Normal Incidence Photodetectors

**Byoung-Whi Kim, Eun-Chang Choi, Kwon Chul Park, and Seok-Youl Kang**

## CONTENTS



## ABSTRACT

We extend our previous theoretical analysis of electronic and optical properties of p-type quantum well structures based on the two heavy- and light-hole system to include all the three valence bands. These theories are then used to clarify the origin of the normal incidence absorption and photocurrent at photon wavelengths of 2 - 3 $\mu$m, which was observed in addition to the absorption around 8 $\mu$m by a recent experimental investigation with heavily doped p-type GaAs/AlGaAs multi-quantum well (MQW) structures. In the theoretical analysis, the Hartree and exchange-correlation many-body interactions are taken into account within one-particle local density approximation, and it is shown that normal incidence absorption occurs in two wavelength regions over the transition energy range higher than barrier height for p-type GaAs/AlGaAs superlattices with well doping of $2 \times 10^{19}$ cm$^{-3}$; one region has broad absorption peaks with coefficients of about 5000 cm$^{-1}$ around 8 $\mu$m, and the other has two rather sharp peaks at 2.7 $\mu$m and 3.4 $\mu$m with 1800 cm$^{-1}$ and 1300 cm$^{-1}$, respectively. The result indicates that the theory explains the experimental observation well, as the theoretical and experimental results are in close agreement in general absorption features.

# I. INTRODUCTION

For infrared imaging arrays it is desirable to use photodetector devices that are sensitive to normal incident light. Due to the intermixing between the heavy, light, and spin split-off hole states, intersubband transitions in the valence band of p-type doped quantum confined structures are allowed and produce significant absorption under normal incident illumination. Hence p-type GaAs/AlGaAs multiple quantum well (MQW) structures are of interest for normal incidence infrared photodetectors. Furthermore, as the hole effective masses are larger than the electron effective mass, p-type MQW structures can be doped more heavily than n-type structures and thereby enhance intersubband absorption without a concomitant increase of the photodiode dark current. However, because of the complexity of the valence band, the intersubband transitions in p-type MQW structures are not well understood at the present time, especially for heavily doped p-type MQWs, despite many good theoretical [1]-[9] and experimental [10]-[14] reports. In order to optimize the photodetector properties, it is important to have a detailed understanding of the absorption processes.

The properties of p-type GaAs/AlGaAs superlattices (SLs) were reported in great detail for normal incident detection in the light of the results of a theoretical investigation of optical absorption in heavily doped SLs including the Hartree and exchange-correlation many body effects [7], [9], treated based on the one-particle local density approximation [15], [16]. As were reported previously for n-type quantum well (QW) structures [17]-[21], it was demonstrated that these many-body effects significantly change the electronic structure and must be taken into account for hole densities in the QW exceeding $p > 10^{18}$ $cm^{-3}$ in order to have a proper structural design [7]-[9]. However, our previous analyses were carried out based on the theory developed in the framework of the two heavy-hole (HH) and light-hole (LH) band system.

It should be noted that although the local density-functional approximation applied for the present calculation has shown a great empirical success in calculating electronic structures for heterojunction systems, the conditions for its validity is seldom obeyed in physical systems of interest [22]. One of problems in applying the local-density-functional formalism to the calculation of the electronic structure is to take into account the image interaction effect arising from the difference in the dielectric constants. However, in typical GaAs-AlGaAs heterostructures the change in dielectric constant is order of 10 % or less and consequently the image interaction is much smaller than the direct Coulomb interaction. Thus for the GaAs/AlGaAs system these image effects can be safely ignored. The rapid variation of the effective mass in going from one side of the interface to the other side also arises fundamental questions about validity of the effective-mass approximation on which the density-functional scheme is applied. This problem may be reduced for SLs, as in SLs the artificial periodicity defines new

effective masses throughout the SL growth direction. In particular, the validity of local-density-functional approximation requires that the electron density variation be small over distances of the order of a Fermi wavelength. For the present situation, the Fermi energy is well above the lowest hole energy and corresponding Fermi wavelength is about 12 Å which is smaller than the well size of 56 Å. Although one cannot safely assume that hole density varies slowly enough on the scale of the Fermi wavelength, it is clear that the situation is more appropriate for applying the approximation as compared with many other situations with 2-dimensional systems reported previously. Nevertheless it will be interesting to explore the corrections to the exchange-correlation effects by going beyond this approximation. This itself, however, requires a significant amount of work and is enough to be an independent subject. Thus the errors in using the approximation may not be easy to measure at the present time. It is certain that employing the approximation should not act against the results, because we all know that exchange-correlation interactions overall lower the particle energies and so does the approximation. Moreover these errors may well be overshadowed by the uncertainty in our knowledge of material parameters. As the principal purpose of the present work is to clarify the origin of the mid-wavelength infrared photoabsorption by calculating some representative values based on our theoretical frame, therefore it would be good enough to use the approximation as far as results with this scheme can indicate whether or not our present suggestion explains the experimental observation.

Very recent experimental and theoretical investigations [13], [14] of infrared absorption in heavily doped p-type ($N_A \sim 2 \times 10^{19}$ cm$^{-3}$) GaAs/AlGaAs MQW structures showed that there are two new absorption peaks at 2.0 $\mu$m and 2.4 $\mu$m with effective normal incidence (ENI) coefficients of 4000 cm$^{-1}$ and 2800 cm$^{-1}$, respectively, in addition to rather broad absorption in the 7-9 $\mu$m range. The ENI absorption coefficient includes multiple passes of light due to internal reflections (Evaluation of this effect indicates that the EIN absorption is about three times larger than the conventional absorption coefficient [13], [14]). A significant photoresponse was also observed around this wavelength range. It was also shown that the observed absorption in the 7 - 9 $\mu$m is attributed principally to the transitions between HH and LH subbands. However the detailed origin of mid-wavelength absorption was not clarified. An ideal photodetector should operate in both the 2-5 $\mu$m and 8-12 $\mu$m wavelength regions. Thus it is timely to further investigate normal incidence intersubband optical absorption (IOSA) mechanisms for the p-type MQWs.

To this end, we extend our previous theoretical analysis [9] of optical transitions in p-type QW structures to include all the three valence bands (the heavy-hole, the light-hole, and the spin split-off bands) and to clarify the origin of the mid-wavelength absorption.

The model SL structure for the theoret-

ical investigation consists of 56 Å well-300 Å barrier SLs with barrier height of 150 meV for both heavy- and light-hole band edge and the spin-split-off band edge [23]. The Hartree and exchange-correlation many-body effects are taken into account within the one-particle local density approximation for both electronic and optical properties calculations. It is noted that an analysis has been carried out on depolarization and exciton-like effects on the intersubband optical transition property of p-type SLs [24] within a linear response approximation [25], and showed that both effects are negligible for the optical transitions of our interest in this article and they are not included in the analysis. Other parameters for the investigation are chosen to be the same as those for the experiment [13], [14]: the doping density is $2 \times 10^{19}$ cm$^{-3}$ in the wells; Carbon is assumed to be the p-type dopant atom [26] (the C atoms are assumed to be fully ionized); and the computations are performed at a temperature of 77 K.

Section II briefly reviews the three-valence-band effective mass equation, and presents a variational calculation method and numerical result of electronic properties, taking into account the Hartree and exchange-correlation many body effects, for the model SLs. Section III extends our previous intersubband optical transition theory for p-type SLs to include the spin split-off hole (SH) band. The theory is then applied to obtain optical properties, such as momentum matrix elements and absorption coefficients, for normal incidence of light.

# II. ELECTRONIC PROPERTIES

## 1. Effective Mass Equation

The effective mass formalism for QW structures [9], [27]-[31] is reconsidered here for use in the p-type SLs including the three HH, LH, and SH bands. In a SL with a periodic effective perturbation $v_{eff}(z)$ only in the z-direction, the one-particle quantum states can be expressed by the in-plane (the plane perpendicular to the z-direction) wave vector $\mathbf{k}_t$ and an index set $(n, q)$ which designates a new quantum state associated with the z-direction, where $n$ is the subband index and $q$ is the SL wave vector. The quantum states of the SL can be expressed by a linear combination of the Bloch wave functions, $|\nu,\ \mathbf{k}\rangle = \exp(i\mathbf{k}\cdot\mathbf{r})u_{\nu,\,\mathbf{k}}(\mathbf{r})$, where $\nu$ is band index in the bulk and $\mathbf{k} = (\mathbf{k}_t,\ k_z)$:

$$|\mathbf{k}_t',\ n,\ q\rangle = \sum_{\nu',\ k_z'} a(\nu',\ \mathbf{k}_t',\ n,\ q;\ k_z')|\nu',\ \mathbf{k}'\rangle. \quad (1)$$

The periodic part of the Bloch wave function, $u_{\nu,k}(\mathbf{k})$, which is correct to first order in the $\mathbf{k}\cdot\mathbf{p}$ perturbation analysis, is given by

$$u_{\nu,\mathbf{k}}(\mathbf{r}) = u_{\nu,0}(\mathbf{r}) + \sum_{L\neq J} \frac{\hbar}{m_0} \frac{\langle u_{L,0}|\mathbf{k}\cdot\mathbf{p}|u_{\nu,0}\rangle}{\varepsilon_\nu^0 - \varepsilon_L^0} u_{L,0}(\mathbf{r}), \quad (2)$$

where $J \equiv \{\nu\}$ is a set of closely located bands in energy, $L$ runs over all the bands except those included in the set of $J$, $m_0$ is the free

electron mass, and $u_{\nu,0}$ and $\varepsilon_\nu^0$ are the lattice periodic function and its corresponding energy at $\mathbf{k}=0$ in band $\nu$ of the bulk, respectively.

Upon substituting (1) and (2) into the equation, we obtain

$$i\hbar\frac{\partial}{\partial t}a(\nu,\mathbf{k}_t,n,q;k_z;t)=\sum_{\nu'}H_{\nu\nu'}(\mathbf{k}_t,k_z)a(\nu',\mathbf{k}_t,n,q;k_z;t)+\sum_{k_z'}V_{k_zk_z'}a(\nu,\mathbf{k}_t,n,q;k_z';t), \tag{3}$$

where,

$$\begin{aligned}\sum_{\nu'}H_{\nu\nu'}(\mathbf{k}_t,k_z)&\equiv\langle\nu,\mathbf{k}|H_0|\mathbf{k}_t',n,q\rangle\\&\cong\left(\varepsilon_\nu^0+\frac{\hbar^2k^2}{2m_0}\right)\delta_{\nu\nu'}+\frac{\hbar}{m_0}\mathbf{k}\cdot\mathbf{p}_{\nu\nu'}+\left(\frac{\hbar}{m_0}\right)^2\sum_{L\neq J}\frac{\langle u_{\nu,0}|\mathbf{k}\cdot\mathbf{p}|u_{L,0}\rangle\langle u_{L,0}|\mathbf{k}\cdot\mathbf{p}|u_{\nu',0}\rangle}{\varepsilon_{\nu'}^0-\varepsilon_L^0}\\&\equiv\sum_{i,j}D_{\nu\nu'}^{ij}k_ik_j,\\\mathbf{P}_{\nu\nu'}&=\langle u_{\nu,0}|\mathbf{p}|u_{\nu',0}\rangle,\\V_{k_zk_z'}&=\int dze^{-ik_zz}v_{eff}(z)\;e^{ik_z'z}.\end{aligned} \tag{4}$$

Here, the Kane's bilinear coefficients of k, $D_{\nu\nu'}^{ij}$, [32] are introduced for future use, $H_0$ is the Hamiltonian of the bulk, and $i,\ j=x,\ y,\ z$.

Taking the Fourier transform of (3) with respect to $k_z$, we obtain a general expression for the one-particle envelope function equation of $\Psi(z)$:

$$i\hbar\frac{\partial}{\partial t}\Psi(\nu,\mathbf{k}_t,n,q;z;t)=\sum_{\nu'}H_{\nu\nu'}(\mathbf{k}_t,-i\partial_z)\Psi(\nu',\mathbf{k}_t,n,q;z;t)+v_{eff}(z)\Psi(\nu,\mathbf{k}_t,n,q;z;t). \tag{5}$$

The effective potential $v_{eff}$ consists of

$$v_{eff}(z)=v_{sq}(z)+v_{ht}(z)+v_{xc}(z), \tag{6}$$

with $v_{sq}$ being the square SL potential, $v_{ht}$ the Hartree potential, and $v_{xc}$ the exchange-correlation potential. The specific forms of these potentials were discussed in ref. [9] in great detail. Note that (5) and (6) form a set of self-consistent equations, as $v_{eff}(z)$ is a function of the square modulus of the envelope function. Due to the periodicity of the SL with a period d, the envelope function $\Psi(z)$ can be replaced by $e^{iqz}\phi(\mathbf{k}_t,\ n,\ q;\ z)$ to obey the Bloch condition, where the periodic part $\phi$ satisfies $\phi(\mathbf{k}_t,\ n,\ q;\ z+d)=\phi(\mathbf{k}_t,\ n,\ q;\ z)$.

As electronic and optical properties of p-type quantum well systems are of our major interest, we include only the valence bands (HH, LH, and SH bands) in the multiband envelope function formalism. The proper inclusion of Luttinger parameters ($\gamma_1,\ \gamma_2,\ \gamma_3=7.65,\ 2.41,\ 3.28$) into the formulas

will compensate for not including bands further in energy (e.g. the conduction bands) in the $\mathbf{k}\cdot\mathbf{p}$ expansion [33]. In this case, (5) can be expressed by a $6\times 6$ matrix:

$$\left\{\begin{bmatrix} X & 0 & iS & R & \frac{-1}{\sqrt{2}}S & -i\sqrt{2}R \\ 0 & X & R^* & iS^* & -i\sqrt{2}R^* & \frac{-1}{\sqrt{2}}S^* \\ -iS^* & R & Y & 0 & i\sqrt{2}Q & -\sqrt{\frac{3}{2}}S \\ R^* & -iS & 0 & Y & -\sqrt{\frac{3}{2}}S^* & i\sqrt{2}Q \\ \frac{-1}{\sqrt{2}}S^* & i\sqrt{2}R & -i\sqrt{2}Q^* & -\sqrt{\frac{3}{2}}S & Z & 0 \\ i\sqrt{2}R & \frac{-1}{\sqrt{2}}S & -\sqrt{\frac{3}{2}}S^* & -i\sqrt{2}Q^* & 0 & Z \end{bmatrix} + v_{eff}\mathbf{I}\right\}\begin{bmatrix} \phi_{h1} \\ \phi_{h2} \\ \phi_{l1} \\ \phi_{l2} \\ \phi_{s1} \\ \phi_{s2} \end{bmatrix} = \langle\varepsilon\rangle\begin{bmatrix} \phi_{h1} \\ \phi_{h2} \\ \phi_{l1} \\ \phi_{l2} \\ \phi_{s1} \\ \phi_{s2} \end{bmatrix}, \tag{7}$$

where $h1(h2)$ designates the total magnetic moment $m_j = +3/2(-3/2)$ for heavy holes, $l1(l2)$ designates $m_j = +1/2(-1/2)$ for light holes, $s1(s2)$ designates $m_j = +1/2(-1/2)$ for spin split-off holes, $\mathbf{I}$ is a $6\times 6$ unit matrix, and the elements of the $H_{\nu\nu'}$ matrix are given by

$$\begin{aligned} X &= -\frac{\hbar^2}{2m_0}(\gamma_1-2\gamma_2)\left(\frac{\partial^2}{\partial z^2}+i2q\frac{\partial}{\partial z}-q^2\right)+\frac{\hbar^2}{2m_0}(\gamma_1+\gamma_2)(k_x^2+k_y^2), \\ Y &= -\frac{\hbar^2}{2m_0}(\gamma_1+2\gamma_2)\left(\frac{\partial^2}{\partial z^2}+i2q\frac{\partial}{\partial z}-q^2\right)+\frac{\hbar^2}{2m_0}(\gamma_1-\gamma_2)(k_x^2+k_y^2), \\ Z &= -\frac{\hbar^2}{2m_0}\gamma_1\left(\frac{\partial^2}{\partial z^2}+i2q\frac{\partial}{\partial z}-q^2\right)+\frac{\hbar^2}{2m_0}\gamma_1(k_x^2+k_y^2)+\Delta, \\ Q &= -\frac{\hbar^2}{2m_0}2\gamma_2\left(\frac{\partial^2}{\partial z^2}+i2q\frac{\partial}{\partial z}-q^2\right)-\frac{\hbar^2}{2m_0}\gamma_2(k_x^2+k_y^2), \\ R &= \frac{\hbar^2}{2m_0}\sqrt{3}\left[\gamma_2(k_x^2-k_y^2)-2i\gamma_3k_xk_y)\right], \\ S &= -\frac{\hbar^2}{2m_0}2\sqrt{3}\gamma_3(k_x-ik_y)\left(q-i\frac{\partial}{\partial z}\right). \end{aligned} \tag{8}$$

The basis vectors chosen for (7) and more detailed information on the above equations are given in Appendix A. It should be noted that the quantities of (8) are defined based on hole's point of view; i.e., the signs are changed as compared with those of the original functions defined based on the electron's point of view (Appendix A).

## 2. Variational Calculation

The unknown wave function can be expressed as a linear combination of $n$ basis functions, which form a complete orthonormal set, with corresponding coefficients $c_l^{\nu}$'s. The fact that $\phi(z)$ is periodic

suggests the possibility of expressing $\phi(z)$ as a Fourier series:

$$\Psi(\nu, k_t, n, q; z) = e^{iqz}\phi(\nu, k_t, n, q; z) = e^{iqz}\sum_{l}^{n} c_l^{\nu} e^{i2\pi lz/d}. \tag{9}$$

For $n \to \infty$ the series approaches an exact solution to the effective mass equation. In practice the series is finite but is chosen to be sufficiently long that errors due to the truncation are negligibly small.

According to the variational principle, the energy is determined by

$$\langle\varepsilon\rangle = \frac{\int \Psi(z)^* H\Psi(z)}{\int \Psi(z)^*\Psi(z)}, \tag{10}$$

thus we obtain the relation

$$\langle\varepsilon\rangle \sum_{\nu}\sum_{l}(c_l^{\nu})^* c_l^{\nu} = \sum_{\nu\nu'}\sum_{ll'}(c_l^{\nu})^* c_{l'}^{\nu'} H_{ll'}^{\nu\nu'}. \tag{11}$$

The values of the $c_l^{\nu}$'s, corresponding to a solution of the effective mass equation, occur for

$$\partial\langle\varepsilon\rangle/\partial(c_l^{\nu})^* = 0. \tag{12}$$

Applying this to (11) gives

$$\langle\varepsilon\rangle \begin{bmatrix} c_l^{HH1} \\ c_l^{HH2} \\ c_l^{LH1} \\ c_l^{LH2} \\ c_l^{SH1} \\ c_l^{SH2} \end{bmatrix} = \sum_{l'} \begin{bmatrix} X_{ll'} & 0 & iS_{ll'} & R_{ll'} & \frac{-1}{\sqrt{2}}S_{ll'} & -1\sqrt{2}R_{ll'} \\ 0 & X_{ll'} & R_{ll'}^* & iS_{ll'}^* & -i\sqrt{2}R_{ll'}^* & \frac{-1}{\sqrt{2}}S_{ll'}^* \\ -iS_{ll'}^* & R_{ll'} & Y_{ll'} & 0 & i\sqrt{2}Q_{ll'} & -\sqrt{\frac{3}{2}}S_{ll'} \\ R_{ll'}^* & -iS_{ll'} & 0 & Y_{ll'} & -\sqrt{\frac{3}{2}}S_{ll'}^* & i\sqrt{2}Q_{ll'} \\ \frac{-1}{\sqrt{2}}S_{ll'}^* & i\sqrt{2}R_{ll'} & -i\sqrt{2}Q_{ll'}^* & -\sqrt{\frac{3}{2}}S_{ll'} & Z_{ll'} & 0 \\ i\sqrt{2}R_{ll'}^* & \frac{-1}{\sqrt{2}}S_{ll'} & -\sqrt{\frac{3}{2}}S_{ll'}^* & -i\sqrt{2}Q_{ll'}^* & 0 & Z_{ll'} \end{bmatrix} \begin{bmatrix} c_{l'}^{HH1} \\ c_{l'}^{HH2} \\ c_{l'}^{LH1} \\ c_{l'}^{LH2} \\ c_{l'}^{SH1} \\ c_{l'}^{SH2} \end{bmatrix}, \tag{13}$$

where

$$X_{ll'} = \left[(\gamma_1 - 2\gamma_2)\left(q + \frac{2\pi l'}{d}\right)^2 + (\gamma_1 + \gamma_2)(k_x^2 + k_y^2) + f_0\right]\delta_{ll'} + f_{l-l'}\bar{\delta}_{ll'},$$

$$Y_{ll'} = \left[(\gamma_1 + 2\gamma_2)\left(q + \frac{2\pi l'}{d}\right)^2 + (\gamma_1 - \gamma_2)(k_x^2 + k_y^2) + f_0\right]\delta_{ll'} + f_{l-l'}\bar{\delta}_{ll'},$$

$$Z_{ll'} = \left[\Delta + \gamma_1\left(q + \frac{2\pi l'}{d}\right)^2 + \gamma_1(k_x^2 + k_y^2) + f_0\right]\delta_{ll'} + f_{l-l'}\bar{\delta}_{ll'},$$

$$
\begin{aligned}
Q_{ll'} &= \left[2\gamma_2\left(q+\frac{2\pi l'}{d}\right)^2-\gamma_2(k_x^2+k_y^2)\right]\delta_{ll'},\\
R_{ll'} &= \left[\sqrt{3}\gamma_2(k_x^2-k_y^2)-i2\sqrt{3}\gamma_3 k_x k_y)\right]\delta_{ll'}=[\sqrt{3}\gamma_2(k_x^2-k_y^2)]\delta_{ll'}+i[-2\sqrt{3}\gamma_3 k_x k_y)]\delta_{ll'}\equiv R_{ll'}^{\mathrm{Re}}+iR_{ll'}^{\mathrm{Im}},\\
S_{ll'} &= \left[-2\sqrt{3}\gamma_3(k_x-ik_y)\left(q+\frac{2\pi l'}{d}\right)\right]\delta_{ll'}=\left[-2\sqrt{3}\gamma_3 k_x\left(q+\frac{2\pi l'}{d}\right)\right]\delta_{ll'}+i\left[2\sqrt{3}\gamma_3 k_y\left(q+\frac{2\pi l'}{d}\right)\right]\delta_{ll'}\\
&\equiv S_{ll'}^{\mathrm{Re}}+iS_{ll'}^{\mathrm{Im}}. \qquad (14)
\end{aligned}
$$

Here we use atomic unit (energy and distance in units of Rydberg and Bohr radius, respectively; $\hbar=1$, $m_0=1/2$, thus $\hbar^2/2m_0=1$), $\bar{\delta}_{ll'}=1$ if $l\neq l'$, and $f_k$ are the Fourier coefficients of the periodic potential of SL:

$$V(z)=V(z+d) \text{ and } V(z)=\sum_{k=-n}^{+n} f_k e^{i2\pi kz/d}. \qquad (15)$$

Applying (14) to (13), the effective mass Hamiltonian can be divided into a real and an imaginary parts:

$$H_{ll'}^{vv'}=A+iB, \qquad (16)$$

where $A$ and $B$ are real matrices and given by

$$
A = \begin{bmatrix}
X_{ll'} & 0 & -S_{ll'}^{\mathrm{Im}} & R_{ll'}^{\mathrm{Re}} & \frac{-1}{\sqrt{2}}S_{ll'}^{\mathrm{Re}} & \sqrt{2}R_{ll'}^{\mathrm{Im}}\\
0 & X_{ll'} & R_{ll'}^{\mathrm{Re}} & S_{ll'}^{\mathrm{Im}} & -\sqrt{2}R_{ll'}^{\mathrm{Im}} & \frac{-1}{\sqrt{2}}S_{ll'}^{\mathrm{Re}}\\
-S_{ll'}^{\mathrm{Im}} & R_{ll'}^{\mathrm{Re}} & Y_{ll'} & 0 & 0 & -\sqrt{\frac{3}{2}}S_{ll'}^{\mathrm{Re}}\\
R_{ll'}^{\mathrm{Re}} & +S_{ll'}^{\mathrm{Im}} & 0 & Y_{ll'} & -\sqrt{\frac{3}{2}}S_{ll'}^{\mathrm{Re}} & 0\\
\frac{-1}{\sqrt{2}}S_{ll'}^{\mathrm{Re}} & -\sqrt{2}R_{ll'}^{\mathrm{Im}} & 0 & -\sqrt{\frac{3}{2}}S_{ll'}^{\mathrm{Re}} & Z_{ll'} & 0\\
\sqrt{2}R_{ll'}^{\mathrm{Im}} & \frac{-1}{\sqrt{2}}S_{ll'}^{\mathrm{Re}} & -\sqrt{\frac{3}{2}}S_{ll'}^{\mathrm{Re}} & 0 & 0 & Z_{ll'}
\end{bmatrix} \qquad (17)
$$

and

$$
B = \begin{bmatrix}
0 & 0 & S_{ll'}^{\mathrm{Re}} & R_{ll'}^{\mathrm{Im}} & \frac{-1}{\sqrt{2}}S_{ll'}^{\mathrm{Im}} & -\sqrt{2}R_{ll'}^{\mathrm{Re}}\\
0 & 0 & -R_{ll'}^{\mathrm{Im}} & S_{ll'}^{\mathrm{Re}} & -\sqrt{2}R_{ll'}^{\mathrm{Re}} & \frac{1}{\sqrt{2}}S_{ll'}^{\mathrm{Im}}\\
-S_{ll'}^{\mathrm{Re}} & R_{ll'}^{\mathrm{Im}} & 0 & 0 & \sqrt{2}Q_{ll'} & -\sqrt{\frac{3}{2}}S_{ll'}^{\mathrm{Im}}\\
-R_{ll'}^{\mathrm{Im}} & -S_{ll'}^{\mathrm{Re}} & 0 & 0 & \sqrt{\frac{3}{2}}S_{ll'}^{\mathrm{Im}} & \sqrt{2}Q_{ll}\\
\frac{1}{\sqrt{2}}S_{ll'}^{\mathrm{Im}} & \sqrt{2}R_{ll'}^{\mathrm{Re}} & -\sqrt{2}Q_{ll'} & -\sqrt{\frac{3}{2}}S_{ll'}^{\mathrm{Im}} & 0 & 0\\
\sqrt{2}R_{ll'}^{\mathrm{Re}} & \frac{-1}{\sqrt{2}}S_{ll'}^{\mathrm{Im}} & \sqrt{\frac{3}{2}}S_{ll'}^{\mathrm{Im}} & -\sqrt{2}Q_{ll'} & 0 & 0
\end{bmatrix}. \qquad (18)
$$

Choosing a specific direction such as along the [010] direction, we have $R^{\mathrm{Im}}_{ll'} = S^{\mathrm{Re}}_{ll'} = 0$ as $k_x = 0$. Thus in this case the matrices $A$ and $B$ become

$$A = \begin{bmatrix} X_{ll'} & 0 & -S^{\mathrm{Im}}_{ll'} & R^{\mathrm{Re}}_{ll'} & 0 & 0 \\ 0 & X_{ll'} & R^{\mathrm{Re}}_{ll'} & S^{\mathrm{Im}}_{ll'} & 0 & 0 \\ -S^{\mathrm{Im}}_{ll'} & R^{\mathrm{Re}}_{ll'} & Y_{ll'} & 0 & 0 & 0 \\ R^{\mathrm{Re}}_{ll'} & S^{\mathrm{Im}}_{ll'} & 0 & Y_{ll'} & 0 & 0 \\ 0 & 0 & 0 & 0 & Z_{ll'} & 0 \\ 0 & 0 & 0 & 0 & 0 & Z_{ll'} \end{bmatrix}, \tag{19}$$

$$B = \begin{bmatrix} 0 & 0 & 0 & 0 & -\frac{1}{\sqrt{2}} S^{\mathrm{Im}}_{ll'} & -\sqrt{2} R^{\mathrm{Re}}_{ll'} \\ 0 & 0 & 0 & 0 & -\sqrt{2} R^{\mathrm{Re}}_{ll'} & \frac{1}{\sqrt{2}} S^{\mathrm{Im}}_{ll'} \\ 0 & 0 & 0 & 0 & \sqrt{2} Q_{ll'} & -\sqrt{\frac{3}{2}} S^{\mathrm{Im}}_{ll'} \\ 0 & 0 & 0 & 0 & \sqrt{\frac{3}{2}} S^{\mathrm{Im}}_{ll'} & \sqrt{2} Q_{ll} \\ \frac{1}{\sqrt{2}} S^{\mathrm{Im}}_{ll'} & \sqrt{2} R^{\mathrm{Re}}_{ll'} & -\sqrt{2} Q_{ll'} & -\sqrt{\frac{3}{2}} S^{\mathrm{Im}}_{ll'} & 0 & 0 \\ \sqrt{2} R^{\mathrm{Re}}_{ll'} & -\frac{1}{\sqrt{2}} S^{\mathrm{Im}}_{ll'} & \sqrt{\frac{3}{2}} S^{\mathrm{Im}}_{ll'} & -\sqrt{2} Q_{ll'} & 0 & 0 \end{bmatrix}. \tag{20}$$

It should be noted that the pair of (19) and (20) should produce the same eigenvalues as those from equations obtained by choosing [100] direction due to the symmetry; i.e., $\sigma_{y-z} C_4(x,\ y) = (y,\ x)$ or $S_4(x,\ y) = (-y,\ x)$, where $\sigma_{y-z}$ is the reflection on the y-z plane.

As seen from (16), the effective mass Hamiltonian is complex in general, and thus the variational coefficients $c_l^{\nu}$'s become complex-valued; i.e., $c_l = u_l + i\nu_l$, where $u$ and $\nu$ are real-valued. Thus we obtain a complex eigenvalue problem:

$$(A + iB) \cdot (u + i\nu) = \lambda (u + i\nu), \tag{21}$$

A method to solve the complex eigenvalue problem of (21) is presented in Appendix B.

## 3. Numerical Result

The self-consistent calculation with the effective mass equation [Eq. (11)] and effective potential equation [Eq. (6)] takes as follows [9]: One starts by neglecting both $\nu_{ht}$ and $\nu_{xc}$ to get envelope functions and corresponding energies for each quantum state and the Fermi level for the square well-barrier SL, and then use these values for the evaluation of these two potentials to obtain improved

those quantities. In the present investigation, this procedure proceeds until the difference of the two consecutive values of energy at the ground state ($k_y = 0$, $n = HH1$, $q = 0$) is less than $10^{-3}$ meV.

The eigenvalues and eigenfunctions of the envelope-function equation are solved variationally by expanding the envelope function in terms of 33 orthogonal basis functions, which are chosen as periodic plane waves $\exp(i2\pi lz/d)$, where $l$ is an integer and $d$ is the SL period. Energies and envelope functions can be obtained by numerical diagonalization of $(6 \times 33) \times (6 \times 33)$ matrix for each quantum state $(k_y, n, q)$. Self-consistent calculations with $n = 33$ were found to converge fast enough. In the numerical computations, (1) we neglect some differences in the band parameters for GaAs and AlGaAs and regard the AlGaAs layer as a potential barrier, as the band structure of GaAs and AlGaAs are quite similar [34]; (2) we include first twelve subbands from the bulk HH and LH bands and first four subbands from the bulk SH band; and (3) we ignore the anisotropy in the x-y plane to simplify the computation, which may be a good approximation [35] and leads the two dimensional integration over $\mathbf{k}_t$ to a one-dimensional one. The acceptor energy levels in the quantum well structures have been calculated by the effective mass approximation [36], [37]. These calculations show that the energy of the acceptor levels vary with dopant position and quantum well and barrier thickness′. However, as a starting approximation for the model SL structure we assume full ionization for the acceptor impurities.

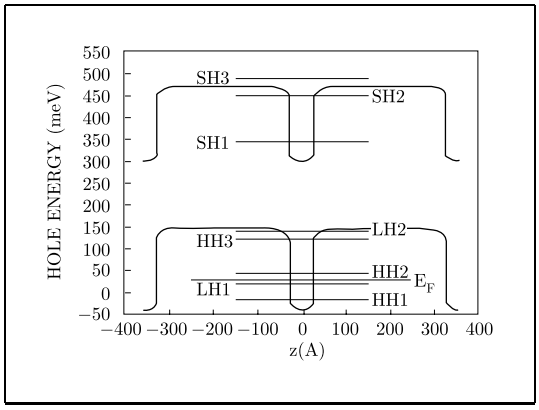


**Fig. 1.** The self-consistent effective potential of the model SL. The Hartree and exchange-correlation many-body effects were taken into account. Shown are 5 subbands from bulk HH-LH band system and 3 subbands from bulk SH band. The Fermi level is located at 28 meV. The doping density is $N_A = 2 \times 10^{19}$ cm$^{-3}$ in the wells.

Fig. 1 shows the self-consistent effective potential of the model SL with doping density of $N_A = 2 \times 10^{-19}$ cm$^{-3}$ in the wells. The Hartree Potential was obtained by integrating the Poisson equation for the resultant self-consistent particle density and ionized acceptor impurity density, and the exchange-correlation potential was obtained by the interpolation formula given by Hedin and Lundquist [16]. As seen from the figure, there is a significant change between the initial square well-barrier and final self-consistent potential shapes; the initial band-edge energy of GaAs, which is set to be zero, is lowered and become negative in the figure. This change

is directly reflected on electronic and optical properties of SLs [9]. In the present doping scheme, exchange-correlation potential makes a major contribution to the change as compared with the Hartree potential. This is because free holes effectively screen the ionized acceptors and make the Hartree potential small.

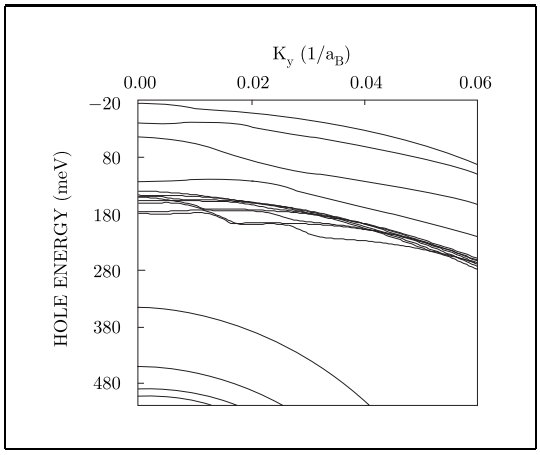


**Fig. 2.** In-plane subband energy structure ($\mathbf{k}_t = k_y$, $q = 0$) of the model SL, where $\mathbf{k}_t$ is the in-plane wave vector and $q$ is the SL wave number. The result was obtained by a self-consistent calculation taking into account many-body effects. The doping density is $N_A = 2 \times 10^{19}$ cm$^{-3}$ in the wells. The subbands in the figure consists of, in the increasing order of the hole energy, HH1, LH1, HH2, HH3, LH2, HH4, HH5, LH3, HH6, HH7, HH8, and LH4 from bulk HH-LH band system; and SH1 - SH4 from bulk SH band. The Fermi level is located at 28 meV.

Fig. 2 and 3 show the self-consistent subband energy structure of the model SL with doping concentration of $N_A = 2 \times 10^{19}$ cm$^{-3}$ in the wells. The energy in-plane wave vector dispersion (Fig. 2) is obtained for $q = 0$, and the energy-SL wave vector dispersion (Fig. 3) is obtained for $\mathbf{k}_t = 0$. The subbands appearing in Fig. 2 are classified into two groups; one group consists of 12 subbands originated from HH-LH bands (HH1, LH1, HH2, HH3, LH2, HH4, HH5, LH3, HH6, HH7, HH8, and LH4 in the increasing order of the hole energy); and the other group of 4 subbands from SH band (SH1 - SH4). The Fermi energy must be also determined self-consistently [9] and is found to be located at 28 meV.

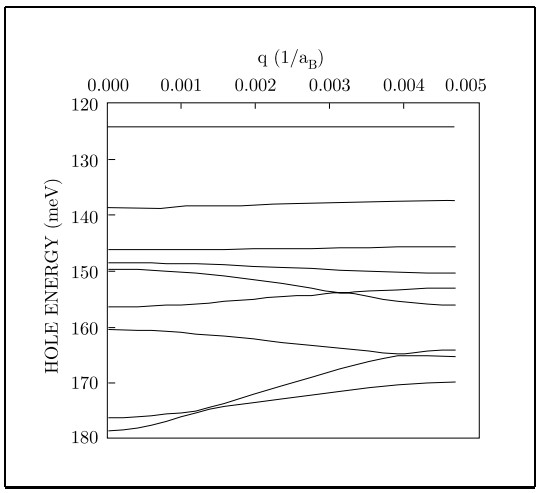


**Fig. 3.** Subband energy structure along the growth direction ($\mathbf{k}_t = 0$, $q$) of the model SL. The results obtained by a self-consistent calculation including many-body effects. The doping density is $N_A = 2 \times 10^{19}$ cm$^{-3}$ in the wells.

Fig. 4(a)-(d) display effective masses along the growth direction. The large effective masses of the bound subbands (subbands below the barriers) indicate a low tunneling probability along the growth direction, which would result in a smaller tunneling component of the dark current in comparison with that

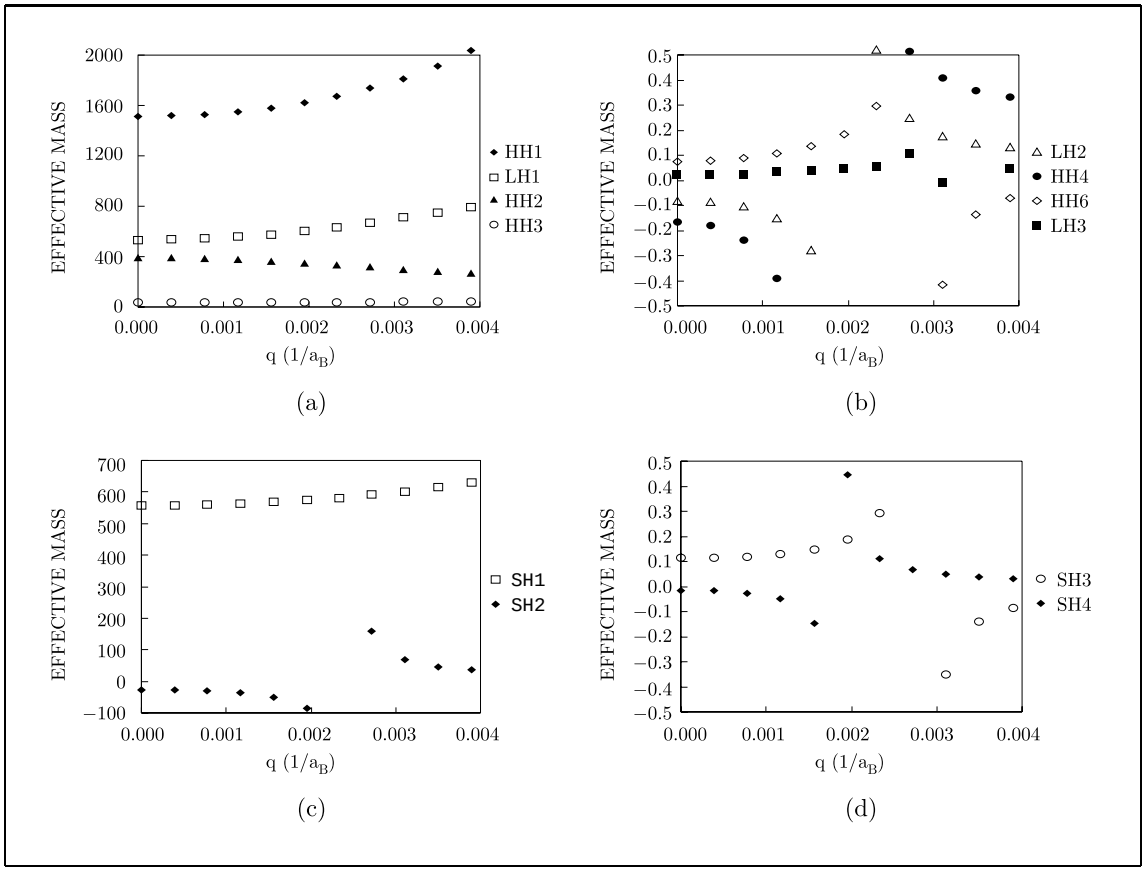


**Fig. 4.** Effective masses of the 12 subbands of interest along the growth direction. The masses were calculated from the self-consistent subband energy structure, in which many-body effects were taken into account. The doping density is $N_A = 2 \times 10^{19}$ cm$^{-3}$ in the wells.

for the n-type QW structures; while the small effective masses of transport subbands (subbands above the barriers) indicate that it is possible to obtain a large improvement in hole mobility and photocurrent along the growth direction by choosing these as the final states of photo- excited holes. As effective masses of those subbands are shown to be in the same order as that of conduction band minimum, it may be possible that the improvement can reach the values that n-type QW structures have shown. It is noted that the effective masses of SH1 and SH2 are very large, which indicates that these subbands are bound. However this region is also taken by subbands originated from HH and LH bands, which forms nearly a continuum in energy. Thus it is expected that the holes photoexcited into the SH subbands can be easily scattered into the continuum and contribute to photocurrent

under the usual external electric field for photodetectors.

Fig. 5 displays hole distributions in the first three HH1, LH1, and HH2 subbands. As the Fermi level is higher than the LH1 subband minimum, significant amount of holes exist in both HH1 and LH1 subbands, but holes in the subbands higher than LH1 are very small and can be neglected. This result indicates that HH1and LH1 make a major contribution, as initial photo excitation states, to the intersubband optical absorption. This will be discussed later.

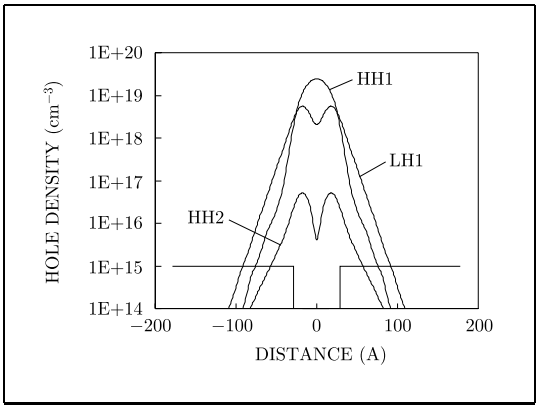


**Fig. 5.** Hole distributions in the first three HH1, LH1, and HH2 subband. The doping density is $N_A = 2\times10^{19}$ cm$^{-3}$ in the wells.

Analysis of envelope function forms is essential to understand in detail why some of the possible optical transitions are stronger than others. Fig. 6 shows the periodic part of the envelope functions of HH1, LH1, SH1, and SH2 for ($\mathbf{k}_t = 0$, $q = 0$) and ($\mathbf{k}_t = 0$, $q = 8\pi/13d$), respectively. The doping density is $2\times10^{19}$ cm$^{-3}$ in the wells. As shown in these figures, the envelope functions at $\mathbf{k}_t = q = 0$ have a definite parity, whereas the envelope functions at $q \neq 0$ do not have a definite parity. In the latter case the real part of the envelope function is even and the imaginary part is odd in z, as discussed in [9]. However even in this case, the dominant symmetry is determined by the symmetry for $q = 0$.

# III. OPTICAL PROPERTIES

## 1. Momentum Matrix Element

In the dipole approximation, the momentum matrix element (MME) of ISOA between the states, $|\mathbf{k}_t, n, q\rangle$ and $|\mathbf{k}_t, n', q\rangle$, is given by

$$\frac{\hbar}{m_0}\langle \mathbf{k}_t, n, q|\hat{\varepsilon}\cdot\mathbf{p}|\mathbf{k}_t, n', q\rangle \equiv \frac{\hbar}{m_0}\hat{\varepsilon}\cdot\mathbf{p}_{nn'}(\mathbf{k}_t, q)$$
$$\equiv \hat{\varepsilon}\cdot\left[\sum_i\sum_{\nu,\nu'} Q^{nn'}_{\nu,\nu'} I^i_{\nu,\nu'}\hat{i} + \sum_i\sum_{\nu,\nu'} R^{nn'}_{\nu,\nu'} J^i_{\nu,\nu'}\hat{i}\right], \tag{22}$$

where $\mathbf{p}$ is the momentum operator, $\hat{\varepsilon}$ is the polarization unit vector of light, direct transitions are assumed (i.e. transitions in which $\mathbf{k}_t$ and $q$ are conserved), and

$$\begin{aligned} Q^{nn'}_{\nu,\nu'} &= \int dz\Psi(\nu, \mathbf{k}_t, n, q; z)^*\Psi(\nu', \mathbf{k}_t, n', q; z), \\ R^{nn'}_{\nu,\nu'} &= \int dz\Psi(\nu, \mathbf{k}_t, n, q; z)^*(-i\partial_z) \\ &\quad \cdot\Psi(\nu', \mathbf{k}_t, n', q; z), \\ I^i_{\nu,\nu'} &= (D^{ix}_{\nu\nu'} + D^{xi}_{\nu\nu'})k_x + (D^{iy}_{\nu\nu'} + D^{yi}_{\nu\nu'})k_y, \\ J^i_{\nu,\nu'} &= (D^{iz}_{\nu\nu'} + D^{zi}_{\nu\nu'}), \end{aligned} \tag{23}$$

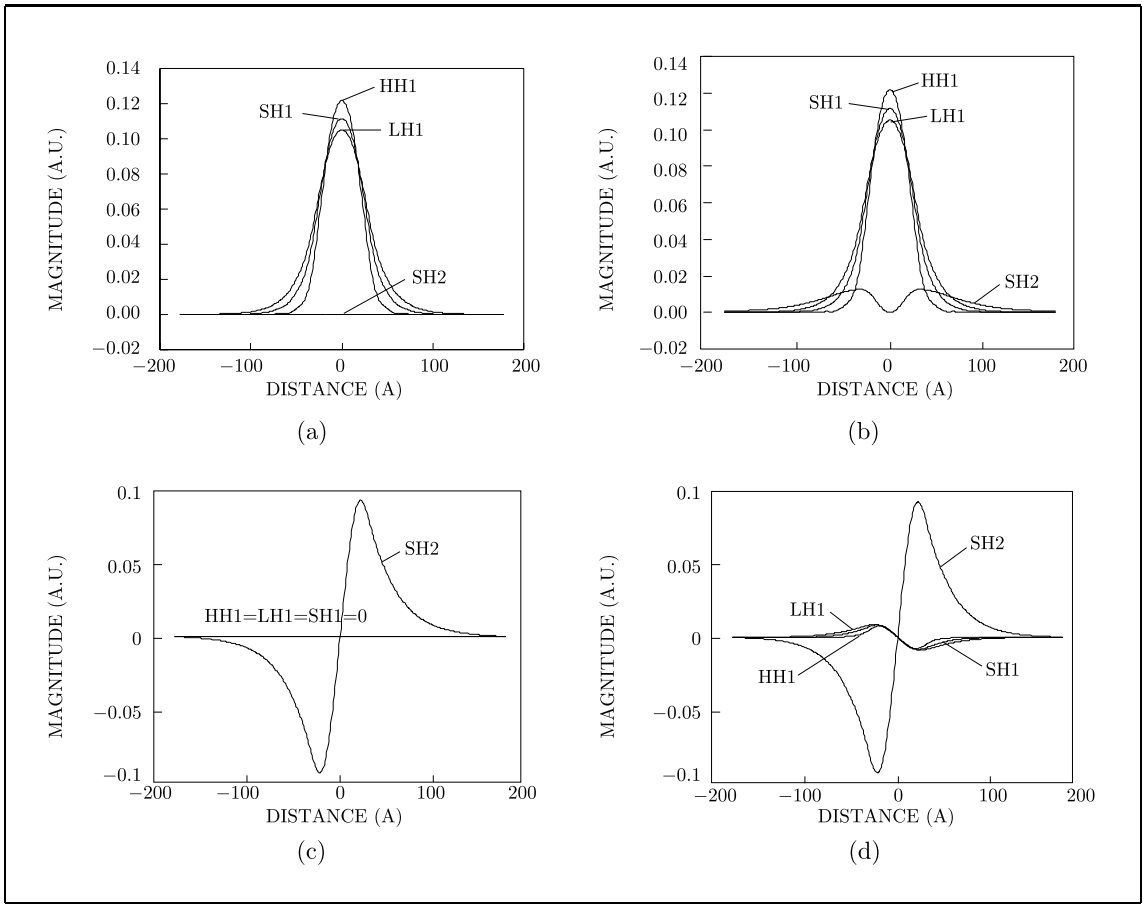


**Fig. 6.** Real and imaginary parts of the periodic part of the 4 envelope functions of interest: (a) real part in ($\mathbf{k}_t = 0$, $q = 0$), (b) real part in ($\mathbf{k}_t = 0$, $q = 8\pi/13d$), (c) imaginary part in ($\mathbf{k}_t = 0$, $q = 0$), and (d) imaginary part in ($\mathbf{k}_t = 0$, $q = 8\pi/13d$). The doping density is $N_A = 2 \times 10^{19}$ cm$^{-3}$ in the wells.

with $i = x, y, z$. The matrices $I^i_{\nu,\nu'}$ and $J^i_{\nu,\nu'}$ are given in Tables I - III. We note that there is a difference (by a factor of 1/2) in the off-diagonal terms in Tables I - III, as compared with those in [1].

Fig. 7 shows MMEs for the transition from HH1 (Fig. 7(a)) and LH1 (Fig. 7(b)) to SH subbands, respectively, for quantum states ($\mathbf{k}_t = k_y$, $q = 0$). As seen in this figure, matrix elements for HH1-SH2 and LH1-SH1 transitions are stronger than others. This is because these subband pairs have favorable respective major symmetries (Fig. 6) for dipole coupling coefficient $R$ of (23), which makes a major contribution to the matrix element in small $k_t$ values. This is directly reflected on the absorption strength in the mid-wavelength range, as shown next.

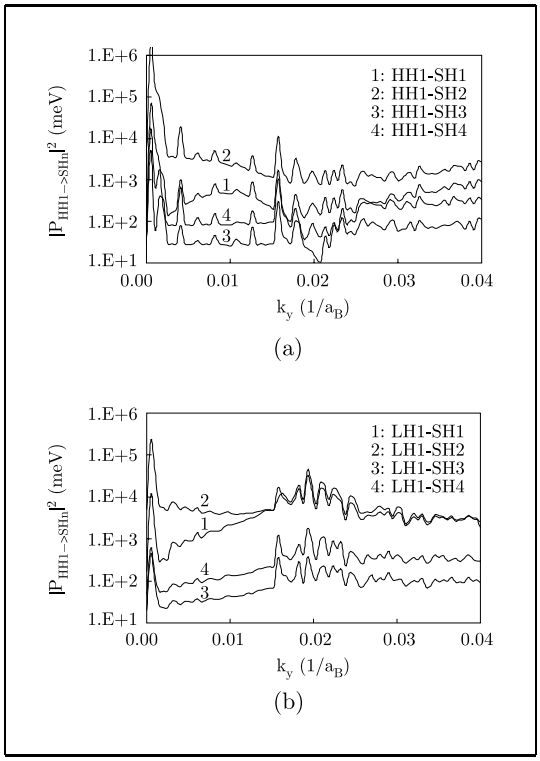


**Fig. 7.** Optical matrix elements of transitions from (a) HH1 and (b) LH1 to SH subbands, respectively, in the states ($\mathbf{k}_t = k_y$, $q = 0$) for light polarized in the y-direction. The matrix elements were calculated based on the electronic structure obtained by a self-consistent calculation including many-body effects. The doping density is $N_A = 2 \times 10^{19}$ cm$^{-3}$ in the wells.

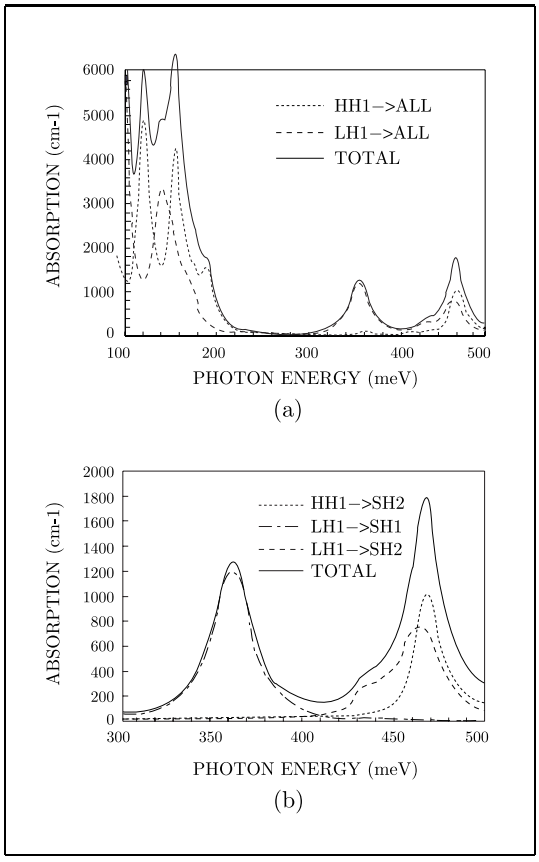


**Fig. 8.** (a) Contribution of holes in HH1 and LH1, respectively, to the total absorption coefficients for normal light incidence to the model SL. (b) Absorption corresponding to HH1-SH2, LH1-SH1, and LH1-SH2 transitions. The doping density is $N_A = 2 \times 10^{19}$ cm$^{-3}$ in the wells. The absorption coefficients were calculated based on the electronic structure obtained by a self-consistent calculation including many-body effects.

## 2. Intersubband Optical Absorption

Within the dipole approximation, the photo-absorption coefficient of the intersubband transition from subband $n$ to $n'$ can be expressed as

$$\alpha_{nn'}(\hbar\omega) = \frac{\pi e^2}{m_0^2 \omega \varepsilon_s c' \Omega} \sum_{\mathbf{k}_t, q} [f_n(\mathbf{k}_t, q) - f_{n'}(\mathbf{k}_t, q)] \times |\hat{\varepsilon} \cdot \mathbf{p}_{nn'}(\mathbf{k}_t, q)|^2 \times \frac{\hbar\Gamma_{nn'}(\mathbf{k}_t, q)}{[\mathcal{E}_{n'}(\mathbf{k}_t, q) - \mathcal{E}_n(\mathbf{k}_t, q) - \hbar\omega]^2 + [\hbar\Gamma_{nn'}(\mathbf{k}_t, q)]^2}, \quad (24)$$

where $\varepsilon_s$, $c'$, $\Omega$ and $f$ are, respectively, the dielectric constant, the speed of light in the mate-

**Table 1.** Elements of $I^x_{v,v'}$ and $J^x_{v,v'}$.

| | | $h1$ | $h2$ | $l1$ | $l2$ | $s1$ | $s2$ |
|---|---|---|---|---|---|---|---|
| $I^x_{v,v'}$ | $h1$ | $(\gamma_1+\gamma_2)k_x$ | 0 | 0 | $\sqrt{3}(\gamma_2 k_x - i\gamma_3 k_y)$ | 0 | $-\sqrt{6}(i\gamma_2 k_x+\gamma_3 k_y)$ |
| | $h2$ | 0 | $(\gamma_1+\gamma_2)k_x$ | $\sqrt{3}(\gamma_2 k_x+i\gamma_3 k_y)$ | 0 | $\sqrt{6}(-i\gamma_2 k_x+\gamma_3 k_y)$ | 0 |
| | $l1$ | 0 | $(\gamma_1-\gamma_2)k_x$ | 0 | $-i\sqrt{2}\gamma_2 k_x$ | 0 | 0 |
| | $l2$ | $\sqrt{3}(\gamma_2 k_x+i\gamma_3 k_y)$ | 0 | 0 | $(\gamma_1-\gamma_2)k_x$ | 0 | $-i\sqrt{2}\gamma_2 k_x$ |
| | $s1$ | 0 | $\sqrt{6}(i\gamma_2 k_x+\gamma_3 k_y)$ | $i\sqrt{2}\gamma_2 k_x$ | 0 | $\gamma_1 k_x$ | 0 |
| | $s2$ | $\sqrt{6}(i\gamma_2 k_x-\gamma_3 k_y)$ | 0 | 0 | $i\sqrt{2}\gamma_2 k_x$ | 0 | $\gamma_1 k_x$ |
| $J^x_{v,v'}$ | $h1$ | 0 | 0 | $-i\sqrt{3}\gamma_3$ | 0 | $\sqrt{\frac{3}{2}}\gamma_3$ | 0 |
| | $h2$ | 0 | 0 | 0 | $-i\sqrt{3}\gamma_3$ | 0 | $\sqrt{\frac{3}{2}}\gamma_3$ |
| | $l1$ | $i\sqrt{3}\gamma_3$ | 0 | 0 | 0 | 0 | $\frac{3}{\sqrt{2}}\gamma_3$ |
| | $l2$ | 0 | $i\sqrt{3}\gamma_3$ | 0 | 0 | $\frac{3}{\sqrt{2}}\gamma_3$ | 0 |
| | $s1$ | $\sqrt{\frac{3}{2}}\gamma_3$ | 0 | 0 | $\frac{3}{\sqrt{2}}\gamma_3$ | 0 | 0 |
| | $s2$ | 0 | $\sqrt{\frac{3}{2}}\gamma_3$ | $\frac{3}{\sqrt{2}}\gamma_3$ | 0 | 0 | 0 |

rial, the volume of the solid, and the Fermi distribution function. $\Gamma_{nn'}(\mathbf{k}_t, q)$ is the linewidth of the transition from $n$ to $n'$ for the state $(\mathbf{k}_t, q)$, which accounts for lifetime broadening due to scattering and inhomogeneity of well widths. In this paper $\hbar\Gamma_{nn'} = 6$ meV is assumed for numerical computations as this value gives a good agreement with our experimental absorption coefficients for low hole concentrations.

Fig. 8(a) shows contribution of holes in HH1 and LH1, respectively, to the total absorption coefficients for normal incidence of light to the model SL. As the holes occupy principally the states in the HH1 and LH1 subbands, only transitions from these to higher subbands were considered. The doping density is $N_A = 2 \times 10^{19}$ cm$^{-3}$ in the wells. As seen in the figure, there appear two peaks at 2.7 $\mu$m and 3.4 $\mu$m with absorption coefficients of 1800 cm$^{-1}$ and 1300 cm$^{-1}$, respectively, in addition to the strong and broad peaks with absorption coefficients of about 5000 cm$^{-1}$ around 8 $\mu$m. Fig. 8(b) shows details of the absorption involving SH subbands. It is shown that the LH1-SH1 transition makes a major contribution to the absorption peak at 3.4 $\mu$m, and transitions of HH1-SH2 and LH1-SH2 to that at 2.7 $\mu$m.

**Table 2.** Elements of $I^y_{\nu,\nu'}$ and $J^y_{\nu,\nu'}$.

| | | $h1$ | $h2$ | $l1$ | $l2$ | $s1$ | $s2$ |
|---|---|---|---|---|---|---|---|
| $I^y_{\nu,\nu'}$ | $h1$ | $(\gamma_1+\gamma_2)k_y$ | 0 | 0 | $-\sqrt{3}(\gamma_2 ky+i\gamma_3 k_x)$ | 0 | $\sqrt{6}(i\gamma_2 k_y-\gamma_3 k_x)$ |
| | $h2$ | 0 | $(\gamma_1+\gamma_2)k_y$ | $\sqrt{3}(-\gamma_2 k_y+i\gamma_3 k_x)$ | 0 | $\sqrt{6}(i\gamma_2 k_y+\gamma_3 k_x)$ | 0 |
| | $l1$ | 0 | $-\sqrt{3}(\gamma_2 k_y+i\gamma_3 k_x)$ | $(\gamma_1-\gamma_2)k_y$ | 0 | $-i\sqrt{2}\gamma_2 k_y$ | 0 |
| | $l2$ | $\sqrt{3}(-\gamma_2 k_y+i\gamma_3 k_x)$ | 0 | 0 | $(\gamma_1-\gamma_2)k_y$ | 0 | $-i\sqrt{2}\gamma_2 k_y$ |
| | $s1$ | 0 | $\sqrt{6}(-i\gamma_2 k_y+\gamma_3 k_x)$ | $i\sqrt{2}\gamma_2 k_y$ | 0 | $\gamma_1 k_y$ | 0 |
| | $s2$ | $-\sqrt{6}(i\gamma_2 k_y+\gamma_3 k_x)$ | 0 | 0 | $i\sqrt{2}\gamma_2 k_y$ | 0 | $\gamma_1 k_y$ |
| $J^y_{\nu,\nu'}$ | $h1$ | 0 | 0 | $-\sqrt{3}\gamma_3$ | 0 | $-i\sqrt{\frac{3}{2}}\gamma_3$ | 0 |
| | $h2$ | 0 | 0 | 0 | $\sqrt{3}\gamma_3$ | 0 | $i\sqrt{\frac{3}{2}}\gamma_3$ |
| | $l1$ | $-\sqrt{3}\gamma_3$ | 0 | 0 | 0 | 0 | $-i\frac{3}{\sqrt{2}}\gamma_3$ |
| | $l2$ | 0 | $\sqrt{3}\gamma_3$ | 0 | 0 | $i\frac{3}{\sqrt{2}}\gamma_3$ | 0 |
| | $s1$ | $i\sqrt{\frac{3}{2}}\gamma_3$ | 0 | 0 | $-i\frac{3}{\sqrt{2}}\gamma_3$ | 0 | 0 |
| | $s2$ | 0 | $-i\sqrt{\frac{3}{2}}\gamma_3$ | $i\frac{3}{\sqrt{2}}\gamma_3$ | 0 | 0 | 0 |

## IV. CONCLUSIONS

We investigated electronic and intersubband optical properties of a p-type GaAs/AlGaAs SL to understand the recent experimental observation of a strong normal-incidence absorption and photocurrent in 2 - 3 $\mu$m wavelength range, in addition to the previously-observed absorption around 8 $\mu$m in heavily doped p-type 56 Å well-300 Å barrier GaAs/$Al_xGa_{1-x}As$ (x=30 %) multi-quantum well structures with doping concentration of $2\times10^{10}$ $cm^{-3}$ in the wells.

For the investigation we first extended our previous theoretical framework for p-type quantum well structures to include all the valence bands (the heavy-hole, the light-hole, and the spin split-off bands). The revised theories were then applied to a p-type SL with the same structural and doping parameters as above in order to analyze the properties such as subband energy structure, particle distribution, symmetry of the envelope functions, and the intersubband optical matrix element and absorption coefficient. The Hartree and exchange-correlation many-body interactions were taken into account in the analysis within one-particle local density approximation.

A comprehensive theoretical analysis was carried out to elucidate the normal incidence mid-wavelength absorption mechanisms in p-

**Table 3.** Elements of $I^z_{\nu,\nu'}$ and $J^z_{\nu,\nu'}$.

| | | $h1$ | $h2$ | $l1$ | $l2$ | $s1$ | $s2$ |
|---|---|---|---|---|---|---|---|
| $I^z_{\nu,\nu'}$ | $h1$ | 0 | 0 | $-\sqrt{3}\gamma_3(ik_x+k_y)$ | 0 | $\sqrt{\frac{3}{2}}\gamma_3(k_x-ik_y)$ | 0 |
| | $h2$ | 0 | 0 | 0 | $\sqrt{3}\gamma_3(-ik_x+k_y)$ | 0 | $\sqrt{\frac{3}{2}}\gamma_3(k_x+ik_y)$ |
| | $l1$ | $\sqrt{3}\gamma_3(ik_x-k_y)$ | 0 | 0 | 0 | 0 | $\frac{3}{\sqrt{2}}\gamma_3(k_x-ik_y)$ |
| | $l2$ | 0 | $\sqrt{3}\gamma_3(ik_x+k_y)$ | 0 | 0 | $\frac{3}{\sqrt{2}}\gamma_3(k_x+ik_y)$ | 0 |
| | $s1$ | $\sqrt{\frac{3}{2}}\gamma_3(k_x+ik_y)$ | 0 | 0 | $\frac{3}{\sqrt{2}}\gamma_3(k_x-ik_y)$ | 0 | 0 |
| | $s2$ | 0 | $\sqrt{\frac{3}{2}}\gamma_3(k_x-ik_y)$ | $\frac{3}{\sqrt{2}}\gamma_3(k_x+ik_y)$ | 0 | 0 | 0 |
| $J^z_{\nu,\nu'}$ | $h1$ | $(\gamma_1-2\gamma_2)$ | 0 | 0 | 0 | 0 | 0 |
| | $h2$ | 0 | $(\gamma_1-2\gamma_2)$ | 0 | 0 | 0 | 0 |
| | $l1$ | 0 | 0 | $(\gamma_1+2\gamma_2)$ | 0 | $i2\sqrt{2}\gamma_2$ | 0 |
| | $l1$ | 0 | 0 | 0 | $(\gamma_1+2\gamma_2)$ | 0 | $i2\sqrt{2}\gamma_2$ |
| | $s1$ | 0 | 0 | $-i2\sqrt{2}\gamma_2$ | 0 | $\gamma_1$ | 0 |
| | $s2$ | 0 | 0 | 0 | $-i2\sqrt{2}\gamma_2$ | 0 | $\gamma_1$ |

type GaAs/AlGaAs SLs. Using the Luttinger Hamiltonian it is shown that the normal incidence mid-wavelength absorption is possible for optical transitions involving HH1, LH1, SH1, and SH2 band states. For non-degenerate and low degenerate hole densities, the Luttinger parameter $\gamma_3$ is of primary importance in this absorption process. On the other hand, for large $k_t$ values the contribution of the $\gamma_2$ times $k_t$ to this absorption coefficient becomes important.

The investigation shows that there are two absorption peaks at 2.7 $\mu$m (467 meV) and 3.4 $\mu$m (361 meV) with absorption coefficients of 1800 and 1300 $cm^{-1}$, respectively, in addition to the predicted strong and broad absorption around 8 $\mu$m with absorption coefficient of about 5000 $cm^{-1}$. The first peak is mainly contributed by the LH1-SH1 transition, and the second by both HH1-SH2 and LH1-SH2. The first experimental observation showed that there are two absorption peaks at 2.0 $\mu$m (620 meV) and 2.4 $\mu$m (520 meV) with evaluated absorption coefficients of 1300 $cm^{-1}$ and 900 $cm^{-1}$, respectively, in addition to the absorption in the 7 - 9 $\mu$m range with evaluated peak coefficient of 1700 $cm^{-1}$. The corresponding photo-current spectrum showed a peak at 2.1 $\mu$m with a shoulder at 2.4 $\mu$m. As the theory and the experiment are in close agreement in general absorption features except detailed values in absorption peak positions (the experimental values shift toward shorter wavelengths by about 150 meV for both absorption peak

positions), we therefore attribute the observed 2 - 3 $\mu$m absorption principally to transitions from HH1 and LH1 to SH1 and SH2. However the "parallel" shift in peak absorption positions between the theory and the experiment needs further clarification and we leave this as a future work. Regarding the photocurrent spectrum, as subbands originated from HH and LH bands form nearly a continuum and coexist with SH subbands in this transition energy region, it would be reasonable to assume that the holes photoexcited into these SH subbands can be easily scattered into the HH and LH continuum and contribute to photocurrent under the usual external electric field for photodetectors. This may explain the recent experimental photo-current observation in this transition energy range.

Finally, in addition to more favorable properties of p-type MQWs as compared with n-type, including a relatively slower degradation of the dark current with increasing doping density and higher absorption values that can be achieved with heavily doped p-type superlattices, it was shown that (1) absorption peaks are well separated in the range of photon energy 2 $\mu$m -10 $\mu$m, and corresponding absorption coefficients are large for normal incidence of light; and (2) the effective masses of the transport subbands are in the same order of that of the conduction band minimum, which is directly reflected in the gain of the photodetector. Therefore p-type GaAs/AlGaAs SL structures appear to be very attractive candidates for multi-color normal incidence photodetectors.

## ACKNOWLEDGEMENTS

We thank Dr. A. Majerfeld, Mr. E. Mao, Mr. S. Dickey for valuable discussions. We wish to acknowledge Dr. C. H. Yim for supporting this work.

## APPENDIX A

The Lödin perturbation theory has been used to calculate the interaction matrices for a six-band $\mathbf{k}\cdot\mathbf{p}$ model of p-type superlattice structure. The Löwdin class-A basis states are chosen as

$$\begin{aligned} \nu_1 &= |X\rangle \sim \{x,\ yz\}, \\ \nu_2 &= |Y\rangle \sim \{y,\ zx\}, \\ \nu_3 &= |Z\rangle \sim \{z,\ xy\}, \end{aligned} \tag{A1}$$

where, due to lack of inversion symmetry, each basis function may be represented by an odd function (the first function in the brace) and an even function (the second one) on the inversion operation. The perturbation term in the Hamiltonian without spin-orbit interaction is $H_{\mathbf{kp}} = \hbar\mathbf{k}\cdot\mathbf{p}/m$ . Thus the corresponding perturbed eigenfunctions can be expressed as

$$\nu_i^{\mathbf{k}} = \nu_i + \frac{\hbar}{m_0}\mathbf{k}\cdot\sum_{nj}\frac{|n\Gamma j\rangle\langle n\Gamma j|\mathbf{p}|\nu_i\rangle}{\mathcal{E}_\nu - \mathcal{E}_{n\Gamma}}, \tag{A2}$$

where the label $\Gamma$ specifies the irreducible representation of the $T_d$ single group, $j$ labels the row to which the function belongs, and $n$ specifies the bands not included in the class-A. Because of the time reversal symmetry of the Hamiltonian without spin-orbit interaction, we are allowed to take these functions, $\nu_i$, to be

real and we make use of this simplification. In (A2) $\mathcal{E}_\nu$ is the eigen energy of the eigen system and $\mathcal{E}_{n\Gamma}$ is the energy of the n*th* band at $\mathbf{k}=0$.

The perturbation matrix in this representation has the form

$$\langle \nu_i | H_{\mathbf{kp}} | \nu_j \rangle = \frac{\hbar^2}{m_0^2} \sum_{nj} \frac{\langle \nu_i | \mathbf{k}\cdot\mathbf{p} | n\Gamma j \rangle \langle n\Gamma j | \mathbf{k}\cdot\mathbf{p} | \nu_j \rangle}{\mathcal{E}_\nu - \mathcal{E}_{n\Gamma}}, \tag{A3}$$

as in the absence of spin-orbit interaction the matrix elements of $\mathbf{p}$ among $|\nu_i\rangle$ states are all zero due to time reversal symmetry: This matrix element could be non-zero because of lack of inversion symmetry of $|\nu_i\rangle$; e.g.,

$$\begin{aligned} \langle \nu_1 | p_z | \nu_2 \rangle &= \langle \{x, yz\} | p_z | \{y, zx\} \rangle \\ &= \langle x | p_z | zx \rangle + \langle yz | p_z | y \rangle \neq 0. \end{aligned}$$

However $\langle \nu_1 | p_z | \nu_2 \rangle = \langle \nu_2 | p_z | \nu_1 \rangle$ by a reflection in the (110) plane, but by partial integration $\langle \nu_1 | p_z | \nu_2 \rangle = -\langle \nu_2 | p_z | \nu_1 \rangle$, as $\nu_i$ functions can be taken to be real due to time reversal symmetry; hence all such matrix elements vanish. Note that when the Hamiltonian includes the spin-orbit interaction, it does not have time reversal symmetry; in this case let $\nu_i \rightarrow w_i \equiv a_i + ib_i$ with real-valued $a_i$ and $b_i$, then by the same reflection operation

$$\begin{aligned} \langle a_1 + ib_1 | p_z | a_2 + ib_2 \rangle &= \int (a_1 - ib_1)\, p_z (a_2 + ib_2) \\ &= \langle a_2 + ib_2 | p_z | a_1 + ib_1 \rangle \\ &= \int (a_2 - ib_2)\, p_z (a_1 + ib_1), \end{aligned}$$

but since, unlike the former case, the partial integration does give

$$\langle a_1 + ib_1 | p_z | a_2 + ib_2 \rangle \neq -\langle a_2 + ib_2 | p_z | a_1 + ib_1 \rangle,$$

thus there exist non-zero matrix elements between the states $w_i$.

The matrix element of (A3) forms $3\times3$ matrix:

$$\begin{array}{c} \quad |X\rangle \qquad\qquad\qquad |Y\rangle \qquad\qquad\qquad |Z\rangle \\ \left[\begin{array}{ccc} E_\nu^0 + M(k_y^2+k_z^2) & Nk_xk_y & Nk_xk_z \\ +Lk_x^2+\hbar^2k^2/2m_0 & & \\ Nk_xk_y & E_\nu^0 + M(k_x^2+k_z^2) & Nk_yk_z \\ & +Lk_y^2+\hbar^2k^2/2m_0 & \\ Nk_xk_z & Nk_yk_z & E_\nu^0 + M(k_y^2+k_z^2) \\ & & +Lk_z^2+\hbar^2k^2/2m_0 \end{array}\right] \end{array}. \tag{A4}$$

The Kane parameters that enter into (A4) are defined by

$$\begin{aligned} L &= F + 2G, \\ M &= H_1 + H_2, \\ N &= F - G + H_1 - H_2, \\ F &= \frac{\hbar^2}{2m_0^2} \sum_{nj} \frac{|\langle x | p_x | n\Gamma_1 j \rangle|^2}{E_\nu - E_{n\Gamma_1}}, \\ G &= \frac{\hbar^2}{2m_0^2} \sum_{nj} \frac{|\langle x | p_x | n\Gamma_3 j \rangle|^2}{E_\nu - E_{n\Gamma_3}}, \\ H_1 &= \frac{\hbar^2}{2m_0^2} \sum_{nj} \frac{|\langle x | p_y | n\Gamma_5 j \rangle|^2}{E_\nu - E_{n\Gamma_5}}, \\ H_2 &= \frac{\hbar^2}{2m_0^2} \sum_{nj} \frac{|\langle x | p_y | n\Gamma_4 j \rangle|^2}{E_\nu - E_{n\Gamma_4}}. \end{aligned} \tag{A5}$$

The parameters in (A5) are taken to be constants by approximating the exact eigenvalue $\mathcal{E}_\nu$ by the non-coupling valence band energy $\mathcal{E}_\nu^0$, and the sums are over all single group states, $|n\Gamma j\rangle$, of the specified irreducible representation, excluding the states in the three-dimensional manifold, $|X\rangle$, $|Y\rangle$, and $|Z\rangle$.

When the spin-orbit interaction is added to the $\mathbf{k}\cdot\mathbf{p}$ perturbation, the energy matrix with

respect to the spin-orbit perturbation is diagonalized by a unitary transformation within the class-A states, using the Clebsch-Gordan coupling coefficients. These transformed basis functions correspond to $\Gamma_7$ and $\Gamma_8$ irreducible representations of the $T_d$ double group and can be chosen as

$$\begin{aligned}
u^{\Gamma_8}_{3/2} &= \frac{1}{\sqrt{2}}(|x\rangle + i|y\rangle)\chi_\uparrow,\\
u^{\Gamma_8}_{-3/2} &= \frac{1}{\sqrt{2}}(i|x\rangle + |y\rangle)\chi_\downarrow,\\
u^{\Gamma_8}_{1/2} &= \frac{1}{\sqrt{6}}(i|x\rangle - |y\rangle)\chi_\downarrow - i\sqrt{\frac{2}{3}}|z\rangle\chi_\uparrow,\\
u^{\Gamma_8}_{-1/2} &= \frac{1}{\sqrt{6}}(|x\rangle - i|y\rangle)\chi_\uparrow + \sqrt{\frac{2}{3}}|z\rangle\chi_\downarrow,\\
u^{\Gamma_7}_{1/2} &= \frac{1}{\sqrt{3}}(|x\rangle + i|y\rangle)\chi_\downarrow + \frac{1}{\sqrt{3}}|z\rangle\chi_\uparrow,\\
u^{\Gamma_7}_{-1/2} &= \frac{1}{\sqrt{3}}(-i|x\rangle - |y\rangle)\chi_\uparrow + \frac{i}{\sqrt{3}}|z\rangle\chi_\downarrow \qquad \text{(A6)}
\end{aligned}$$

The spin-orbit interaction $H_{so} = \hbar/4m^2c^2[\nabla V \times \mathbf{p}]\cdot\sigma$ is diagonal in the double group basis class-A states $u_j$, taking the values $\Delta/3$ and $-2\Delta/3$, where $\Delta$ is defined below. In the new basis $u_j$, the matrix element of $\mathbf{k}\cdot\mathbf{p}$ and spin-orbital interactions, $\langle u_i|H_{\mathbf{kp}} + H_{so}|u_j\rangle$, is given by

$$\begin{array}{c}
\begin{array}{cccccc} u^{\Gamma_8}_{+3/2} & u^{\Gamma_8}_{-3/2} & u^{\Gamma_8}_{+1/2} & u^{\Gamma_8}_{-1/2} & u^{\Gamma_7}_{+1/2} & u^{\Gamma_7}_{-1/2} \end{array}\\
\begin{bmatrix}
X & 0 & iS & R & \frac{-1}{\sqrt{2}}S & -i\sqrt{2}R\\
0 & X & R^* & iS^* & -i\sqrt{2}R^* & \frac{-1}{\sqrt{2}}S^*\\
-iS^* & R & Y & 0 & i\sqrt{2}Q & -\sqrt{\frac{3}{2}}S\\
R^* & -iS & 0 & Y & -\sqrt{\frac{3}{2}}S^* & i\sqrt{2}Q\\
\frac{-1}{\sqrt{2}}S^* & i\sqrt{2}R & -i\sqrt{2}Q^* & -\sqrt{\frac{3}{2}}S & Z & 0\\
i\sqrt{2}R^* & \frac{-1}{\sqrt{2}}S & -\sqrt{\frac{3}{2}}S^* & -i\sqrt{2}Q^* & 0 & Z
\end{bmatrix}
\end{array}, \qquad \text{(A7)}$$

where elements in this matrix are given by

$$\begin{aligned}
X &= E_\nu - (\gamma_1+\gamma_2)\frac{\hbar^2}{2m_0}(k_x^2+k_y^2) - (\gamma_1-2\gamma_2)\frac{\hbar^2}{2m_0}k_z^2,\\
Y &= E_\nu - (\gamma_1-\gamma_2)\frac{\hbar^2}{2m_0}(k_x^2+k_y^2) - (\gamma_1+2\gamma_2)\frac{\hbar^2}{2m_0}k_z^2,\\
Z &= E_\nu - \Delta - \gamma_1\frac{\hbar^2}{2m_0}(k_x^2+k_y^2+k_z^2),\\
Q &= \gamma_2\frac{\hbar^2}{2m_0}(k_x^2+k_y^2-2k_z^2),\\
R &= -\frac{\hbar^2}{2m_0}\sqrt{3}[\gamma_2(k_x^2-k_y^2) - 2i\gamma_3 k_x k_y],\\
S &= \frac{\hbar^2}{2m_0}2\sqrt{3}\gamma_3 k_z(k_x - ik_y),\\
\mathcal{E}_\nu &= \mathcal{E}^0_\nu + \frac{\Delta}{3},\\
\frac{\Delta}{3} &= -i\frac{\hbar}{4m_0^2c^2}\langle x|(\nabla V_0 \times \mathbf{p})_y|z\rangle,\\
\gamma_1 &= -\frac{2}{3}\frac{m_0}{\hbar^2}(L+2M) - 1,\\
\gamma_2 &= -\frac{1}{3}\frac{m_0}{\hbar^2}(L-M),\\
\gamma_3 &= -\frac{1}{3}\frac{m_0}{\hbar^2}N. \qquad \text{(A8)}
\end{aligned}$$

Finally, based on (A7), the effective mass equation for holes in the two-dimensional structure can be made as (7) on replacing $k_z$ by $-i\partial_z$.

## APPENDIX B

As the effective mass Hamiltonian is complex in general, the variational coefficients $c_l$'s to express unknown periodic SL wave function $\phi(z)$ becomes complex-valued; i.e., $c_l = u_l + i\nu_l$, where $u$ and $\nu$ are real-valued. Thus we obtain a complex eigenvalue problem:

$$(A+iB)\cdot(u+i\nu) = \lambda(u+i\nu), \qquad \text{(B1)}$$

where $A$ and $B$ are square $n \times n$ real matrices, and $u$ and $v$ are real $n \times 1$ eigenvectors. It can be easily seen that the above $n \times n$ complex eigenvalue problem is equivalent to the $2n \times 2n$ real eigenvalue problem:

$$\begin{bmatrix} A & -B \\ B & A \end{bmatrix} \begin{bmatrix} u \\ v \end{bmatrix} = \lambda' \begin{bmatrix} u \\ v \end{bmatrix}, \qquad \text{(B2)}$$

where the $2n \times 2n$ matrix is symmetric, because of the Hermitian condition

$$(A+iB)^{\dagger} = (A+iB), \qquad \text{(B3)}$$

which implies

$$A^T = A \text{ and } B^T = -B. \qquad \text{(B4)}$$

Introducing a unitary matrix $w$,

$$w = \begin{bmatrix} 1 & -i \\ -i & 1 \end{bmatrix}, \qquad \text{(B5)}$$

it satisfies

$$w \begin{bmatrix} A & -B \\ B & A \end{bmatrix} w = \begin{bmatrix} A+iB & \\ & A-iB \end{bmatrix}, \qquad \text{(B6)}$$

Multiplying both sides of (B2) by $w$ from the left gives

$$\begin{bmatrix} A+iB & \\ & A-iB \end{bmatrix} \begin{bmatrix} u+iv \\ i(u-iv) \end{bmatrix} = \lambda \begin{bmatrix} u+iv \\ i(u-iv) \end{bmatrix}$$

or

$$\begin{cases} (A+iB)(u+iv) = \lambda_1 (u+iv) \\ (A-iB)(u-iv) = \lambda_2 (u-iv) \end{cases}, \qquad \text{(B7)}$$

where $w^{\dagger} w = 1$ is used. Here $\lambda_1 = \lambda_2$, which can be seen from the fact that complex conjugate of the upper equation equals the lower equation. Therefore the 2n eigenvalues of this augmented problem of (B2) are given by

$$\lambda_1, \lambda_1, \lambda_2, \lambda_2, \lambda_3, \lambda_3, \cdots, \lambda_n, \lambda_n, \qquad \text{(B8)}$$

and the eigenvectors are pairs of the form

$$u+iv \quad \text{and} \quad i(u-iv). \qquad \text{(B9)}$$

Thus we choose one eigenvalue and eigenvector from each pair.

## REFERENCES


[1] Y. C. Chang and R. B. James, Phys. Rev. B 39, 12672 (1989)

[2] D. Teng, C. Lee, and L. F. Eastman, J. Appl. Phys. 72, 1539 (1992)

[3] H. Xie, J. Katz, and W. I. Wang, Appl. Phys. Lett. 59, 3601 (1991);

[4] H. Xie, J. Katz, and W. I. Wang, J. Appl. Phys. 71, 2844 (1992)

[5] H. H. Chen, M. P. Houng, Y. H. Wang, and Y. C. Chang, Appl. Phys. Lett. 61, 509 (1992)

[6] P. Man and D. S. Pan, Appl. Phys. Lett 61, 2799 (1992)

[7] B. W. Kim and A. Majerfeld. GaAs and Related Compounds 1993. Inst. Phys. Conf. Ser. No 136, pp 307 [1994].

[8] A. Majerfeld, Z. H. Lu, B. W. Kim, E. Mao, S. A. Dickey, and E. G. Oh, Proceedings of the First International Symposium on Long Wavelength Infrared Detectors, 184th Electrochemical Society Meeting. New Orlenas, Louisiana. October 1993.

[9] B. W. Kim and A. Majerfeld, J. Appl. Phys. 77, 4552 (1995)

[10] B. F. Levine, S. D. Gunapala, J. M. Kuo, S. S. Pei, and S. Hui, Appl. Phys. Lett. 59, 1864(1991)

[11] J. S. Park, R. P. G. Karunasiri, and K. L. Wang, Appl. Phys. Lett. 61, 681 (1992)

[12] S. D. Gunapala, B. F. Levine, D. Ritter, R. Hamm, and M. B. Panish, J. Appl. Phys. 71, 2458 (1992)

[13] E. Mao, S. A. Dickey, B. W. Kim, A. Majerfeld, R. Melliti, and P. Tronc, NANOSTRUCT'96 (1996)

[14] E. Mao, S. A. Dickey, B. W. Kim, and A. Majerfeld, ICMOVPE'96 (1996)

[15] W. Kohn and L. J. Sham, Phys. Rev. 140, 1133 (1965)

[16] L. Hedin and B. I. Lundqvist, J. Phys. C 4, 2064 (1971)

[17] Y. C. Chang and G. D. Sanders, Phys. Rev. B 32, 5521 (1985)

[18] K. M. S. V. Bandara, D. D. Coon, Byungsung O, Y. F. Lin, and M. H. Francombe, Appl. Phys. Lett 53, 1931 (1988)

[19] W. L. Bloss, J. Appl. Phys. 66, 3639 (1989)

[20] J. W. Choe, Byungsung O, K.M.S.V. Bandara, and D.D. Coon, Appl. Phys. Lett. 56, 1679 (1990)

[21] M.O. Manasreh, F. Szmulowicz, T. Vaughan, K.R. Evans, C.E. Stutz, and D.W. Fischer, Phys. Rev. B 43, 9996 (1991)

[22] F. Stern and S. D. Sarma, Phys. Rev. B 30, 840 (1984)

[23] S. Adachi, Gallium arsenide (Key papers in Physics No. 1), pp. 73, edited by J. S. Blakemore, American Institute of Physics, 1987

[24] B. W. Kim, unpublished.

[25] T. Ando, Solid State Comm. 21, 133 (1977)

[26] M. C. Hanna, Z. H. Lu, and A. Majerfeld, Appl. Phys. Lett. 58, 164 (1991)

[27] W. Potz, W. Porod, and D.K. Ferry, Phys. Rev. B, 32, 3868 (1985)

[28] G. Bastard and J. A. Brum, IEEE J. Q.E. 22, 1625 (1986)

[29] H. Luo and J. K. Furdyna, Phys. Rev. B 41, 5188 (1990)

[30] N. F. Johnson, H. Ehrenreich, P.M. Hui, and P.M. Young, Phys. Rev. B 41, 3655 (1990)

[31] J. B. Xia, S. F. Ren, and Y. C. Chang, Phys. Rev. B 43, 1692 (1991)

[32] E. O. Kane, J. Phys. Chem. Solids 1, 82 (1956)

[33] P. Lawaetz, Phys. Rev. B 4, 3460 (1971)

[34] T. Ando, J. Phys. Soc. Jap. 54, 1528 (1985)

[35] T. C. Chang and J.N. Schulman, Phys. Rev. B 31, 2069 (1985)

[36] W. T. Masselink, Y.C. Chang, and H. Morkoc, J. Vac. Sci. Technol. B 2, 376 (1984)

[37] G. P. Srivastava, Theory of impurity states in superlattice semiconductors NATO ASI Series B: Physics Vol.183, pp. 195, Plenum Press, New York (1988)

**Byoung-Whi Kim** received a Ph.D. degree in electrical and computer engineering from University of Colorado, Boulder, Colorado in 1993. From 1983 to 1988, he was involved in the development of a digital switching system in ETRI. Since he joined ETRI again in 1994, he has been working on III-V compound-semiconductor optical switches based on the strain-induced piezoelectric effects. His research interests include theoretical physics of compound semiconductor materials and optoelectronic devices.

**Eun-Chang Choi** received B.S. and M.S. degrees in electronics engineering from Kyungpook National University in 1990 and 1992, respectively. He has worked at the Korea Atomic Energy Research Institute from 1992 to 1993. He joined ETRI in 1994, where he is currently working as a member of engineering staff of ATM Switching Section. His research interests include high speed VLSI design, PLL and CAD.

**Kwon Chul Park** earned BSEE, MSEE, and Ph.D. degrees in electronics engineering at the University of Korea in 1977, 1979, and 1988, respectively. He has worked for ETRI since 1982 and was originally involved in the development of the TDX switching system where he worked for the development of the T1 interface circuits, the network synchronization equipment and digital switch of the TDX system. In 1992 he became involved in the development of the TDX-ATM switching system. Currently he is Head of the ATM Switching Section in ETRI.

**Seok Youl Kang** for photograph and biography, see this issue, p. 244.